Reconstructing Equatorial Electron Flux Measurements from low-Earth-orbit: A Conjunction Based Framework

D.L. Stumbaugh[1], J. Bortnik[1], and S.G. Claudepierre[1]

[1]University of California, Los Angeles

Corresponding author: Dominique Stumbaugh (dstumbaugh@ucla.edu)

Key Points:

- A dataset of 64,200 conjunctions and a neural network is used to predict equatorial flux measurements for > 30 keV electrons
- The conjunction-trained neural network requires low-Earth-orbit electron fluxes, *L* and MLT, and AE measurements as sole inputs
- Out-of-sample reconstruction of electron flux measurements agree well with Van Allen Probes observations, $R^2 > 0.8$

Abstract

We present an artificial neural network (ANN) model that reconstructs > 30 keV electron flux measurements near the geomagnetic equator from low-Earth-orbit (LEO) observations, exploiting the global coherent nature of the high-energy trapped electrons that constitute the radiation belts. To provide training data, we analyze magnetic conjunctions between one of National Oceanic and Atmospheric Administration's (NOAA's) Polar Orbiting Environmental Satellites (POES) and National Aeronautics and Space Administration's (NASA's) Van Allen Probes. These conjunctions occur when the satellites are connected along the same magnetic field line and allow for a direct comparison of satellites' electron flux measurements for one integral energy channel, > 30 keV and over 64,000 such conjunctions have been identified. For each conjunction, we fit the equatorial pitch angle distribution (PAD) parameterized by the function $J_D = \mathrm{C} \cdot \sin^N \alpha$. The resulting conjunction dataset contains the POES electron flux measurements, L and MLT coordinates, geomagnetic activity AE index, and C and N coefficients from the PAD fit for each conjunction. We test combinations of input variables from the conjunction dataset and achieve the best model performance when we use all the input variables during training. We present our model's prediction for the out-of-sample data that agrees well with observations, $R^2 > 0.80$. We demonstrate the ability to nowcast and reconstruct equatorial electron flux measurements from LEO without the need for an in-situ equatorial satellite. The model can be expanded to include existing LEO data and has the potential to be used as a basis of future radiation-belt monitoring LEO constellations.

Plain Language Summary

We present a machine learning model trained on a dataset that uses the global coherent nature of the radiation belts to reconstruct electron flux measurements. We establish conjunctions, or times, when the National Oceanic and Atmospheric Administration's Polar Orbiting Environmental Satellites (POES) and the National Aeronautics and Space Administration's Van Allen Probes are connected along the same magnetic field line and measuring the same electron population. Our conjunction dataset contains electron flux measurements, positional coordinates, and geomagnetic activity measurements. We use the conjunction dataset to train our machine learning model to reconstruct equatorial electron flux measurements. We show that the model

performs well for data it was not trained on. Our current work demonstrates that we can monitor in situ radiation belt fluxes using only relatively smaller and cost-effective satellites with a neural network model instead of the more traditional high-altitude satellites. The ability to predict radiation belt dynamics, and thus space weather, has become increasingly important for the broader society due to an increasing satellite infrastructure that is vulnerable to energetic electrons.

1 Introduction

The Earth's Van Allen radiation belts are dynamic regions of trapped, energetic charged particles (Schulz & Lanzerotti, 1974; Van Allen et al., 1958). Violation of the adiabatic invariants induces competing transport, acceleration, and loss processes which greatly affect the radiation belts' structure (Reeves et al., 2003). Under quiet conditions, the radiation belts have a two-zone structure with a well-defined slot region between the belts around L = 2, the McIlwain (1961) parameter that labels geomagnetic field lines by their approximate equatorial crossing radii. Under active conditions, when geomagnetic storm and substorm activity is intensified, the slot region is filled as energetic particles are injected into the Earth's inner magnetosphere and accelerated locally within this region by radial diffusion and wave-particle interactions (Li & Hudson, 2019; Reeves et al., 2016). Recovery from this enhanced state has been attributed to electron loss caused by pitch angle diffusion into the loss cone resulting from wave-particle interactions as well as outward radial diffusion to the magnetopause (Li & Hudson, 2019; Lyons et al., 1972; Thorne et al., 2013).

The subsequent precipitation of electrons can interfere with satellite systems by gradually degrading electronic systems onboard (Lanzerotti et al., 1998; DeForest, 1972). The National Aeronautics and Space Administration (NASA) Van Allen Probes (formerly known as the Radiation Belt Storm Probes, RBSP) were launched in August 2012 to understand how charged particles evolve within the radiation belts. While the mission concluded in 2019, its electron flux measurements are well calibrated and validated (Claudepierre et al., 2021; Mauk et al., 2013). RBSP's Magnetic Electron Ion Spectrometers (MagEIS), while pitch-angle resolved, were nevertheless limited in pitch angle (α) coverage, particularly for precipitating electron fluxes, with the minimum observed equatorial pitch angle (α_{eq}) being greater than 10 - 20 degrees

(Claudepierre et al., 2021). Additionally, with only two probes, RBSP was at times limited in its spatiotemporal coverage of the radiation belts due to the probes' spacing and geostationary transfer orbit (GTO) at any given point during its operation (Mauk et al., 2013). On the other hand, satellites in low-Earth-orbit (LEO), such as the National Oceanic and Atmospheric Administration (NOAA) Polar Orbiting Environmental Satellites (POES), do not have the same limitations. At present, POES contains five spacecraft in polar orbit covering different magnetic local time (MLT) swaths, each with the ability to measure deep within the loss cone while covering the entire radiation belt region roughly four times per 100 minute orbit (Evans, 2000). Therefore, POES' measurements are complementary to RBSP's and can be used to measure and study electron precipitation in a way that is not accessible to RBSP (e.g., H. Chen et al., 2023; Fung et al., 1996; Lazaro et al., 2022; Rodger et al., 2010a). Furthermore, during active times, changes to the equatorial pitch angle distributions of electrons as measured from a GTO-style orbit are reflected in LEO measurements, as particles diffuse to lower pitch angles. This leads to a global coherence between all pitch-angles, and can be observed between the two sets of measurements (Kanekal et al., 2001).

Machine learning (ML) has become an increasingly common method in reconstructing electron fluxes and can be used for further exploiting the relationship between GTO and LEO observations (Camporeale, 2019). Even before the launch of RBSP, neural networks were being used to reconstruct GTO on the limited data available at the time (e.g., Fukata et al., 2002; Kitamura et al., 2011; Koons & Gorney, 1991; Ling et al., 2010). Since the launch of RBSP and the large quantity of high-resolution, well-calibrated data that it produced, neural networks have been used in reconstructing and forecasting primarily relativistic electrons (Botek et al., 2023; Chu et al., 2021; Ma et al., 2022; Pires de Lima et al., 2020; Zhelavskaya et al., 2021). For example, Y. Chen et al. (2019) developed the PreMevE model that forecasts 1 MeV spin-averaged electron flux distributions spanning hours to 1-day from POES to LANL GEO. Updates to the PreMevE include work by Pires de Lima et al. (2020) on PreMevE 2.0 and by Sinha et al. (2021) on PreMevE2E that focus on other ML methods and a further prediction (2-day) time window. Other works investigate both non-relativistic and relativistic energy channels. The SHELLS model was developed by Claudepierre & O'Brien (2020) and updated by Boyd et al. (2023) and is a neural network with nowcasting ability for 1-min averaged 350 keV and 1 MeV electron fluxes using POES inputs. The model uses spin-averaged flux, and the updated version

incorporates radial, angular, and energy dependence to allow for user specification of the electron environment. The authors note that the current SHELLs model is unlikely to capture rapid (< 1 min) temporal changes (Boyd et al., 2023).

In our study, we build upon and extend these earlier studies by using flux measurements from POES to nowcast RBSP at a much lower energy range, electrons > 30 keV, for times when POES and RBSP are in magnetic conjunction. We use windows in L, MLT, and time to establish magnetic conjugacy between the low-altitude POES and the geostationary RBSP. Figure 1 illustrates a typical magnetic conjunction at $L = 4$ (described further in Section 2.2). By establishing magnetic conjunctions, we investigate times when the two satellites are connected along the same magnetic field line and can therefore provide a more complete equatorial pitch angle distribution (PAD) as the two satellites measure the same, streaming electron populations. Electrons at energies of > 30 keV play an important role in seeding local acceleration processes (Jaynes et al., 2015); during heightened geomagnetic activity, tens to hundreds of keV electrons are injected into the inner magnetosphere from the magnetotail and can supply energy to excited chorus waves that accelerate ~100s keV electrons to multi-MeV energies over the following few hours through resonant wave-particle interactions. Despite magnetic conjunctions between RBSP and POES occurring frequently, using them to establish a ML training set for energies as low as ~30 keV has not yet been done to the best of the author's knowledge. In this study, we demonstrate that an artificial neural network (ANN) model trained on our conjunction dataset can accurately predict equatorial flux measurements for the outer radiation belt at > 30 keV, using only LEO based electron flux measurements, LEO satellite ephemeris data, and geomagnetic indices (i.e., AE). This allows for the nowcasting of GTO from potentially any LEO satellite at any time resolution without the need for large, expensive, in situ GTO missions such as RBSP.

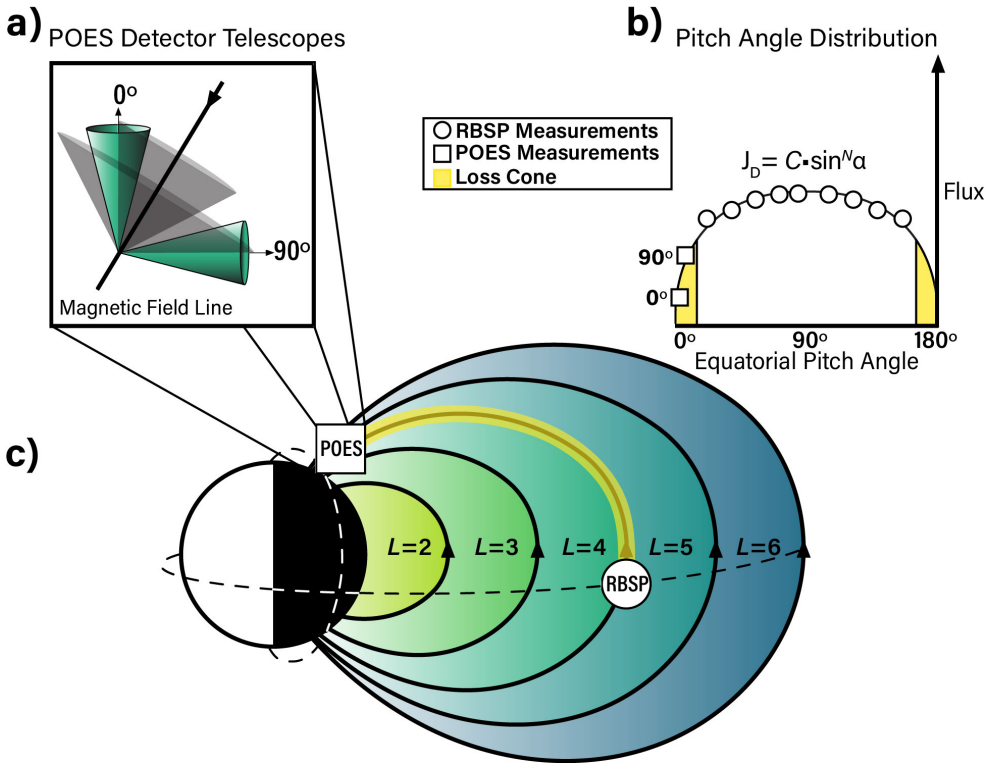

Figure 1. Schematic showing RBSP in conjunction with POES. (a) POES 90º and 0º Detector Telescopes' orientation with respect to the magnetic field line for a specific latitude. Note that throughout POES' orbits, the angle of the two detector telescopes with respect to the magnetic field line will change. (b) Equatorial Pitch Angle Distribution from the innermost nine RBSP pitch-angle bins (circles) together with the and POES 90º and 0º (squares) that cover the lowest pitch angle range. The distribution is fitted using the simple function $J_D = \mathrm{C} \cdot \sin^N \alpha$, a scaled sine function. The loss cone is shown in yellow at the ends of the distribution. (c) POES in low-Earth-orbit and RBSP in a geostationary transfer orbit magnetically conjuncted on the nightside along L = 4, highlighted by yellow.

2 Data and Methods

In section 2.1, we introduce the data used for our ANN model and the two satellites we use in our study, one in GTO and one from LEO. In section 2.2, we define our conjunction criteria and establish our conjunction data set. In section 2.3, we present our ANN model.

2.1 Instrumentation and Data

In order to obtain the equatorial electron flux measurements, we use data from NASA's Van Allen Probes (RBSP) mission launched in August 2012 and deactivated in 2019 (Mauk et al., 2013). In its time of operation the twin satellites, RBSP-A and RBSP-B, were in a highly

144 elliptical geostationary transfer orbit (GTO) with a perigee of ~600 km and an apogee of ~5.8
145 Earth's Radii (R_E) at ~10° inclinations and with a varying separation between ~0.1 to 5 R_E
146 (Mauk et al., 2013). The Magnetic Electron Ion Spectrometer (MagEIS) sensors on RBSP
147 measured pitch-angle resolved electron flux data with energies ranging from roughly 30 keV to 4
148 MeV at an 11 second spin time cadence (Blake et al., 2013; Spence et al., 2013). For this study,
149 we use level 3 data from MagEIS, which we refer to as 'RBSP', that have been corrected for
150 background contamination (Claudepierre et al., 2015).

151 In order to obtain LEO measurements, we use low-altitude measurements provided by
152 NOAA's POES and the European Organisation for the Exploitation of Meteorological Satellites
153 (EUMETSAT) Meteorological Operational Satellite (MetOp). This network of spacecraft is in
154 near polar, Sun-synchronous orbits at altitudes of roughly 800-850 km with ~100 min orbital
155 periods. Each spacecraft operates in a different magnetic local time (MLT) sector, which
156 together as a network provides extensive spatiotemporal coverage. In our work, we use data from
157 only one spacecraft, the EUMETSAT/METOP-2 spacecraft which we refer to as 'POES' that
158 orbits roughly in the 10-22 MLT meridional plane, for demonstration purposes. The Medium
159 Energy Proton and Electron Detector (MEPED) on POES measures the energetic protons and
160 electrons ranging from 30 keV to 200 MeV via two solid-state detector telescopes at a 2-second
161 time cadence (Evans, 2000; Green, 2013). For this study, we use data from one energy channel,
162 the integral electron channel E1 (> 30 keV). The MEPED sensor has one telescope oriented to
163 the zenith direction (the so-called "0-degree telescope", POES 0) and the other perpendicular to
164 the zenith direction (the so-called "90-degree telescope", POES 90). Only when at the polar
165 regions is this orientation ideal to differentiate precipitating (POES 0) and trapped or quasi-
166 trapped electrons (POES 90) with upper and lower limits with in ±15° viewing (Rodger et al.,
167 2010b, 2010a).

168 In addition to the electron flux measurements, we use the satellites' magnetic ephemeris
169 data (i.e., L-shell value (L) and MLT) defined using the Olson and Pfitzer 1997 (static) quiet
170 field model, OP77 (Olson & Pfitzer, 1977). For geomagnetic index measurements, we use the
171 Auroral Electrojet (AE) Index from the OMNI dataset and retain the AE values over a look-back
172 window of three hours before the conjunction. Since AE measurements are provided at a 5-
173 minute cadence, 36 data points make up this time series for each conjunction.

Predictor	Full Name	Description	Unit
POES 0	$\log_{10}$(POES 0 Flux)	Logarithm of the electron integral flux measured in $cm^{-2}\ s^{-1}\ str^{-1}$	Unitless
POES 90	$\log_{10}$(POES 90 Flux)	Logarithm of the electron integral flux measured in $cm^{-2}\ s^{-1}\ str^{-1}$	Unitless
L	L-shell	Location at which a magnetic field line intersects with the equatorial plane	R_E
MLT	Magnetic Local Time	Local time based on Earth's magnetic field, Midnight = 00 MLT, Noon = 12 MLT	hr
AE	Auroral Electrojet Index	Measure of Auroral Zone Magnetic Activity at time of conjunction, AE(-0min)	nT
AE TS	AE Index Time Series	Look-back window of three hours (5 min cadence) at time of conjunction, AE(-5min) through AE(-175min)	nT

Table 1. Description of the Predictor Variables for the ANN. The variables consist of the logarithmic flux measurements from POES0 and POES90, *L* and MLT of each conjunction, AE at the time of the conjunction, and AE over a look-back window of three hours (36 data points).

2.2 Conjunction Identification Methodology

To ensure that POES and RBSP are connected by the same geomagnetic field line, we define magnetic conjunctions between the two spacecraft based on magnetic and temporal coordinates. Figure 1 shows a schematic view of a single conjunction. To establish magnetic proximity, we use the magnetic ephemeris data of RBSP and POES (i.e., *L* and MLT), using OP77 (Olson & Pfitzer, 1977). We use the OP77 model because it is simple and computationally efficient, yet sufficiently accurate in the inner magnetosphere for our purposes of conjunction identification. While there may be some uncertainty in the low-to-high altitude mapping as result of the OP77 model, other models (e.g., the Tsyganenko model, T89; Tsyganenko, 1989) also introduce uncertainty, since they require solar wind parameters (which are not always available, or may not always produce the geoeffective that is expected), they are not necessarily more accurate in the dipolar regions of the inner magnetosphere, and they take much longer to compute (Yang & Wang, 2021). We interpolated RBSP's magnetic ephemeris data to the same time cadence as POES (2 seconds) since it moves relatively slowly in *L* and MLT compared to POES and set small tolerances in L-shell ($dL < 0.1\ L$) and magnetic local time (dMLT < 0.5 hr) between the two spacecraft to identify conjunctions. Additionally, to establish temporal proximity, we set a tolerance in conjunction time (dt < 5 seconds). Using this approach, we identify 73,831 conjunctions between POES and RBSPA and 73,093 conjunctions between

195 POES and RBSPB between 01-Jan-2014 to 01-Jul-2019.

196 For each identified conjunction, we numerically integrate RBSP's differential fluxes with
197 respect to energy to match POES' integral flux measurements for the > 30 keV channel. To
198 verify the flux measurements, we restrict the RBSP flux measurements to the lowest pitch angle
199 (α) bins within 16 degrees, i.e., $\alpha < 16°$ or $\alpha > 164°$, ensuring that the RBSP flux measurements
200 include fully or nearly precipitating electrons near the loss cone, and thus be the best match with
201 POES fluxes. We compare POES with RBSP integral flux for >30 keV electrons from 01-Jan-
202 2014 to 01-Jul-2019 using a scatterplot in Figure 2. Figure 2a and 2b are colored by L-shell.
203 Figure 2c and 2d are normalized by the bin count and therefore indicate where the data resides in
204 the plot. The plots show that POES 90 (Figure 2a and 2c) is better correlated to RBSP, compared
205 to POES 0 (Figure 2b and 2c), as expected, since these are predominantly trapped fluxes near the
206 edge of the loss-cone. It should also be noted that with RBSP's limited pitch angle coverage,
207 RBSP is measuring a population with a higher pitch angle range compared to POES 90 and 0. As
208 a result, RBSP's flux is most likely dominated by trapped and/or quasi-trapped particles which
209 would degrade the correlation between RBSP and truly precipitating fluxes from POES 0
210 (Rodger et al., 2010b). In addition, fluxes at higher *L* are in better agreement (less spread) than at
211 lower L-shells. This is partly because POES' orientation and viewing with respect to the
212 magnetic field line changes ±15° throughout its orbit and subsequent *L* coverage (Rodger et al.,
213 2010a). A future correction factor may be needed to adjust the POES data.

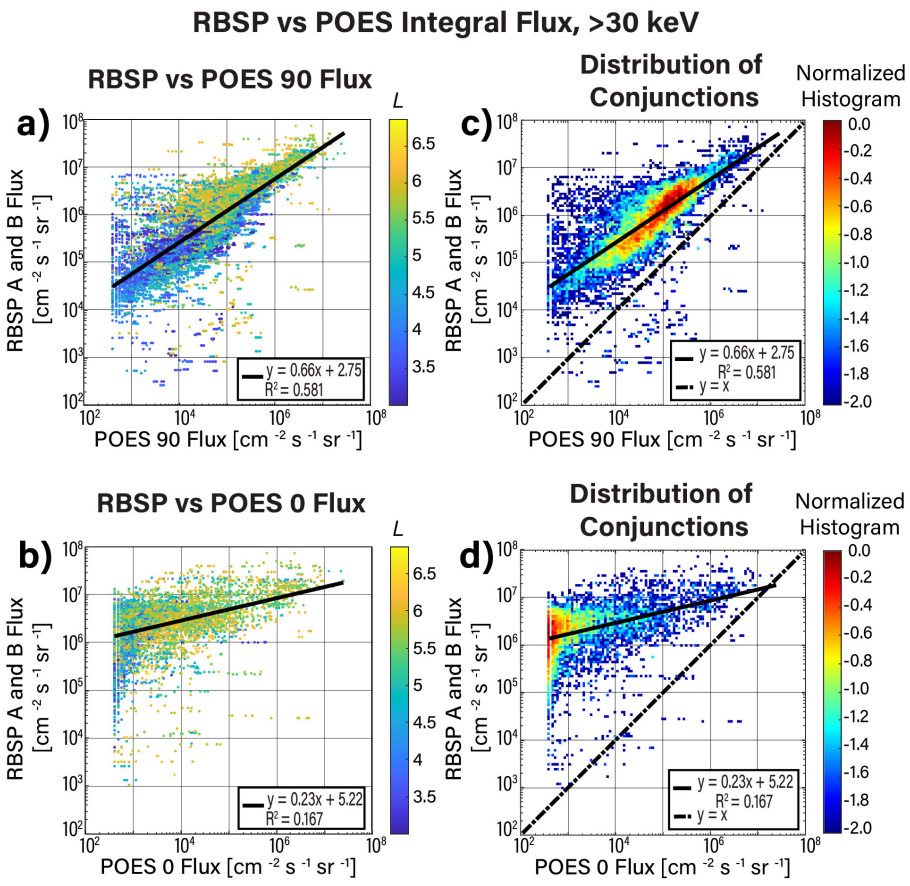

214

215 **Figure 2.** A comparison of RBSP (equatorial) versus POES (LEO) Fluxes. RBSP data is
216 restricted in pitch angle to be the edges of the pitch angle distribution, $\alpha < 16°$ or $\alpha > 164°$, to
217 give the most meaningly comparison, and restricted in flux to be the integral flux matching the
218 POES > 30 keV channel. (a) and (b) are direct comparisons of flux of RBSP to POES90 and
219 POES0, respectively, colored by L-shell. (c) and (d) are the distribution of conjunctions colored
220 by, colored by log10(bin count) of POES90 and POES0, respectively. The normalized histogram
221 values closer to 0 (red) indicate that there are more conjunctions for that bin compared to values
222 closer to -2 (blue).

223 With the identified set of conjunctions and with the flux relationship verified, we are now
224 able to map the POES PA to its equatorial PA and plot the equatorial PAD for each conjunction
225 (refer to the inset panels in Figure 3a for example conjunctions). We assume each conjunction's
226 equatorial PAD to be in the simple form of $J_D = C \cdot \sin^N \alpha$ where the J_D is the unidirectional
227 differential flux and α is the pitch angle, , following previous studies that have found such a
228 functional form to be sufficiently accurate to represent equatorial PADs (Greeley et al., 2024; Gu
229 et al., 2011; Vampola, 1997). Following the method established by Gu et al. (2011), we perform
230 a linear regression to fit each conjunction's equatorial PAD by applying the least squares

method. To do so, we convert $J_D = C \cdot \sin^N \alpha$ from linear to log space, $\log_{10} J_D = \log_{10} C + N \log_{10} (\sin \alpha)$. This becomes a simple linear function where the *C* and *N* coefficients in log space are intercept and slope of the resulting linear relationship, respectively. These coefficients characterize the equatorial PAD and will serve as our ML model's target (output) variables. To ensure representative fitting, we only fit conjunctions with more than eight data points (two from POES and at least six from RBSP). The coefficient of determination (R^2) indicates the quality and amount of variation captured in the linear regression and serves as another quality safeguard for our conjunctions. We set a threshold based on the R^2 value to filter out poorly fit conjunctions.

Each conjunction in our data set is fitted in this manner and the R^2 values are plotted in Figure 3a, against the conjunctions' L-shell value and colored by the $\log_{10}(\text{Flux}_{90^\circ})$, where Flux_{90° refers to the equatorial flux at 90 degrees. To provide a sense of what various distributions might look like, the inset panels in Figure 3a show examples of a poor and a good fit, respectively, based on the coefficient of determination. We note that most of the conjunctions above $L = 3$ are fitted well using this method, which coincides with our region of interest in the outer radiation belt. It should be noted that for the inner zone or regions of $L < 3$, there is much more variability in the R^2 values a dramatic decrease in flux (and therefore the *N* coefficient), indicating contamination by more energetic protons and requiring a different calibrated database (Fung et al., 1996). We plot the mean of the R^2 values for each 0.1 *L* bin as red circles with black outlines, error bars in red indicating the standard deviation. We establish a $R^2 > 0.8$ threshold (red line) to filter out poor fits (e.g. highly peaked, butterfly, or flattop PADs), instead of a hard L-shell cutoff. This threshold maintains suitable L-shell coverage, as shown in Figure 3b, ensures good accuracy and retains a sufficient amount of data for out fitting procedure. The histogram is binned into 0.1 *L* bins and contains the 43,711conjunctions with $R^2 > 0.8$.

In our conjunction dataset, the POES 90 and POES 0 electron flux measurements capture locally mirroring and precipitating electron flux in LEO and the AE index time series captures geomagnetic activity and therefore serve as a proxy for relevant wave-particle interactions. The complete conjunction dataset also includes the POES magnetic ephemeris data (*L* and MLT) and the *C* and *N* coefficients characterizing the equatorial PAD. We thus create a comprehensive dataset focused on electron precipitation, ideal for a ML model.

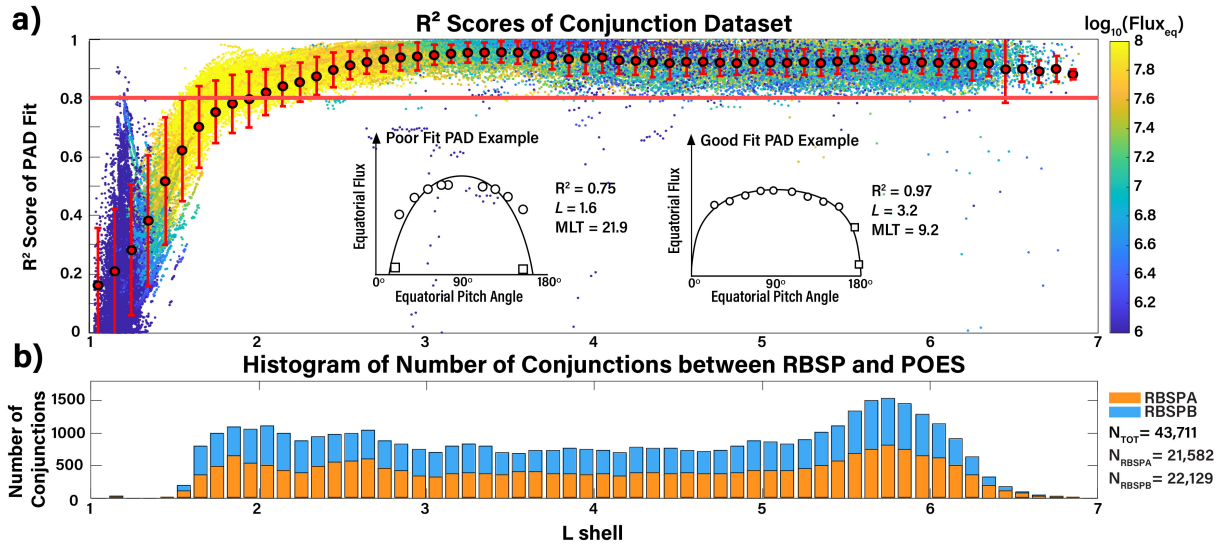

Figure 3. An Overview of the Conjunction Dataset. (a) R^2 scores of the Conjunction Dataset versus L-shell, colored by the logarithmic of the 90 degree equatorial flux ($\log_{10}(Flux_{90°})$). For every 0.1 *L* bin, the mean (red dots) and standard deviation (red bars) of the R^2 score is shown. The inset pitch angle distributions (PADs) show an example of a poor (left) and good (right) PAD fit, based on the R^2 score of the fit. Only conjunctions with a score $R^2 > 0.8$ (above red line) are used for the neural net. (b) Histogram of the number of conjunctions between RBSPA (orange) and RBSPB (blue) with POES above the $R^2 > 0.8$ threshold (depicted as the red line in panel (a)). The total number of conjunctions that meet this criterion is $N_{TOT} = 43{,}711$.

2.3 Neural Network Model

In this study, we use a Multi-layer Perceptron (MLP) Regressor ANN model since these models are able to model nonlinear relationships well including the coupled, physical processes (i.e. global coherence) linking the low and high altitude flux measurements (Bortnik et al., 2016; Hornik et al., 1989). We use only RBSPB in the training of the model, as RBSPB and RBSPA were in nearly identical orbits with the same coverage in *L* and MLT space (Mauk et al., 2013). For preprocessing of the data, we transform POES and RBSPB fluxes into logarithmic space and remove any zero flux values and remove any missing or corrupted (i.e. NaN) values. When we remove NaN values, 5,122 conjunctions are removed from the training set mainly due to the AE index's availability ending in March 2018. We also withhold the year of 2014 from training and reserve it for validation (4,456 conjunctions). Therefore, the training set retains 12,551 conjunctions for the time range 01-Jan-2015 to 01-Mar-2018. We standardize our data to have a zero mean and unit variance following SciKit-Learn's preprocessing module (Pedregosa et al.,

283 2011). We split our conjunction dataset into a train (70%, 8,785 conjunctions) and test (30%,
284 3,766 conjunctions) set.

285 To select the best set of feature values, we begin by investigating feature importance and
286 evaluating the performance of 5 separate models with different permutations of inputs listed in
287 Table 1 and illustrated in Figure 4). To motivate the models' hyperparameter choices, we
288 perform an exhaustive 3-fold cross-validated grid search over the hyperparameters through
289 SciKit-Learn's GridSearchCV optimizer (Pedregosa et al., 2011). We achieve the highest
290 coefficient of determination between the observed and predicted flux (both in training, $R^2 = 0.94$
291 and in testing, $R^2 = 0.96$) when all parameters are used as inputs and (i.e. Model #5). Our
292 resulting feed forward, fully connected ANN contains 40 input neurons which include the POES
293 90 and POES 0 flux measurements, the *L* and MLT coordinates, and the 36 AE data points from
294 the three-hour timeseries described above.

295 The 40 inputs are mapped to the two outputs (the *C* and *N* coefficients from the equatorial
296 PAD fitting defined earlier in section 2.2) via two hidden layers of size 100 nodes each. The
297 ANN uses the rectified linear unit, relu, activation function in the hidden layers and a linear
298 activation function in the output layer. By definition, the MLP Regressor optimizes the squared
299 error using stochastic gradient descent (SGD) with L2 regularization (Pedregosa et al., 2011).
300 Our ANN uses the adaptive moment estimation, Adam, solver which is an extension of SGD that
301 combines the ability of an adaptive learning rate with the ability to deal with sparse gradients
302 (Kingma & Ba, 2017). The selected number of hidden layers and respective nodes, the activation
303 function, and the solver are a result of the hyperparameter optimization of the grid search.

Inputs	***L***	**MLT**	**POES 90**	**POES 0**	**AE**	**AE TS**	**Mean cross-validated R^2 score**
Model #1	x	x	x				0.88
Model #2	x	x	x		x		0.89
Model #3	x	x	x	x			0.90
Model #4	x	x	x	x	x		0.91
Model #5	x	x	x	x	x	x	0.93

304 **Table 2.** Permutations of inputs for the 5 models (corresponding with Figure 4). Model #1 uses
305 *L*, MLT, and POES90 as inputs while Model #5 uses *L*, MLT, POES 90 and 0, and the full AE

timeseries with 36 data points. Last column reports the mean cross-validated coefficient of determination value, R^2, for each model.

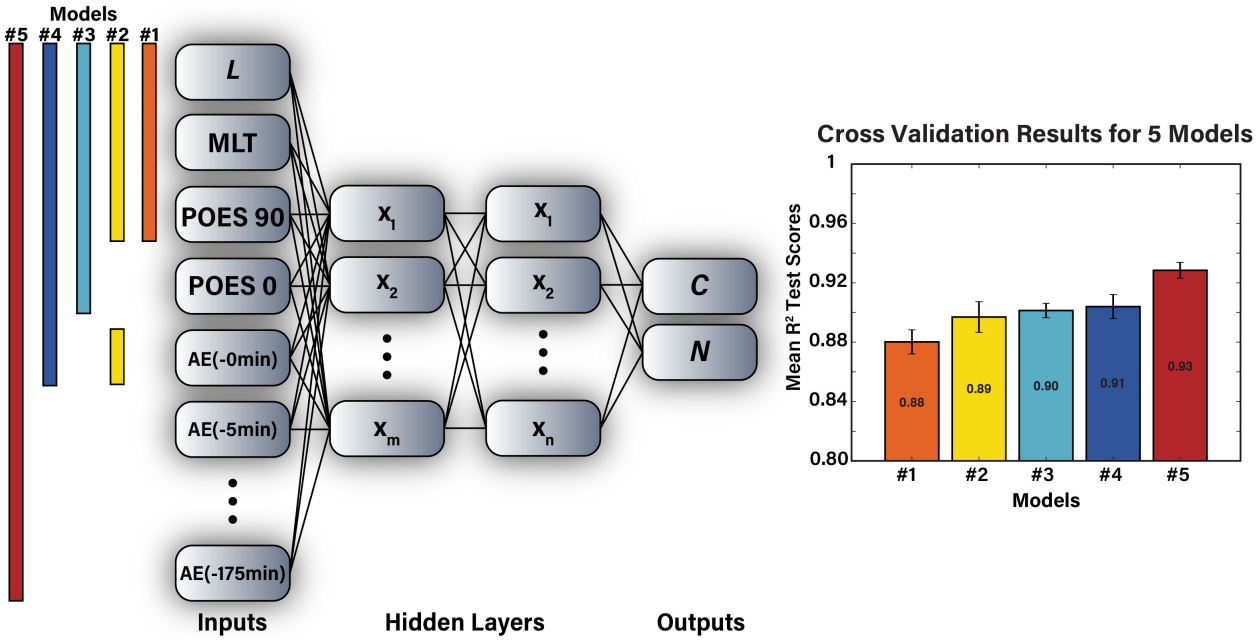

Figure 4. Schematic of the ANN model. Permutations of inputs for the 5 models are denoted by the colored bars on the left side of the schematic. For model #5, there are 40 inputs including L-shell, MLT, POES 90, POES 0, and the AE timeseries. The AE time series represents the AE index taken at a 5-minute cadence over the 3 hour window before the conjunction time, AE(-0 min) through AE(-175 min) resulting in 36 data points. There are 2 hidden layers of size 100 each and 2 outputs, the C and N coefficients from the $J = C \cdot \sin^N \alpha$ fits. Through an exhaustive grid search cross validation of the 5 separate models, the best performance (R^2) was achieved when all 40 inputs were used (i.e. Model #5).

3 Results

The results of our ANN model trained on our conjunction dataset for the out-of-sample validation period (year of 2014) are shown in Figure 5. We note that the first two thirds of the year 2014 (until August) are relatively quiet in terms of geomagnetic activity and the last third of the year (from September onward) contains higher geomagnetic activity. Using 2014, we can evaluate our model's ability to predict out-of-sample GTO fluxes across various levels of geomagnetic activity and the POES time cadence (2 seconds). Figure 5a-c show the (a) observed and (b) predicted 60° Flux and (c) RMSE between Figures 5a and 5b for RBSPB. The flux measurements (Figure 5a) are observed MagEIS integral flux >30 keV equatorial measurements

averaged into 0.1 L and 1-day bins. Due to its off-equatorial orbit, the typical pitch angle of the observations is roughly $\alpha \approx 60°$ (with the average being $\alpha = 55°$). We compare the observed data to the model's (b) predicted ~60° Flux, by using $\alpha = 55°$ and the predicted C and N values for the $J_D = \mathrm{C} \cdot \sin^N \alpha$ fit. We quantify the agreement between (a) observed and (b) predicted with the (c) RMSE between figures 5a and 5b. Figure 5d-5f show the (d) fitted and (e) predicted 90° Fluxes and (f) RMSE between figures 5d and 5e for RBSPB. The flux measurements (Figure 5d) are MagEIS >30 keV equatorial, integral flux measurements fitted in the same way but showing the inferred, strictly equatorial values (that are often not directly observed by RBSP) with α=90°. We can present the equatorial flux at GTO and directly compare it to the output of the model at α_{eq}. As seen in the error metrics, there is good agreement between the (a) observed and (b) predicted 60° electron flux measurements and between the (d) fitted and (e) predicted 90° electron flux measurements.

The regions where agreement is poorer are demarcated with a red contour in Figures 5a and 5c indicating where RMSE > 0.6 for the 60° and 90° Flux values. While these regions could initially suggest that the model is not performing adequately, it should be noted that the large error generally results from areas where the observed flux values are very low. To illustrate this point further, we transfer the red contours directly on to the observed fluxes values (i.e., from Figure 5c to Figure 5a and from Figure 5f to Figure 5d) where it becomes clear that the regions of large RMSE map directly on to regions of low fluxes, and hence small fluctuations in model predictions result in large errors. This trend is also reassuring because the large errors occur in regions that are of less importance from a space weather hazard perspective, whereas regions of high fluxes (and hence important for space weather applications) have low errors and excellent model performance.

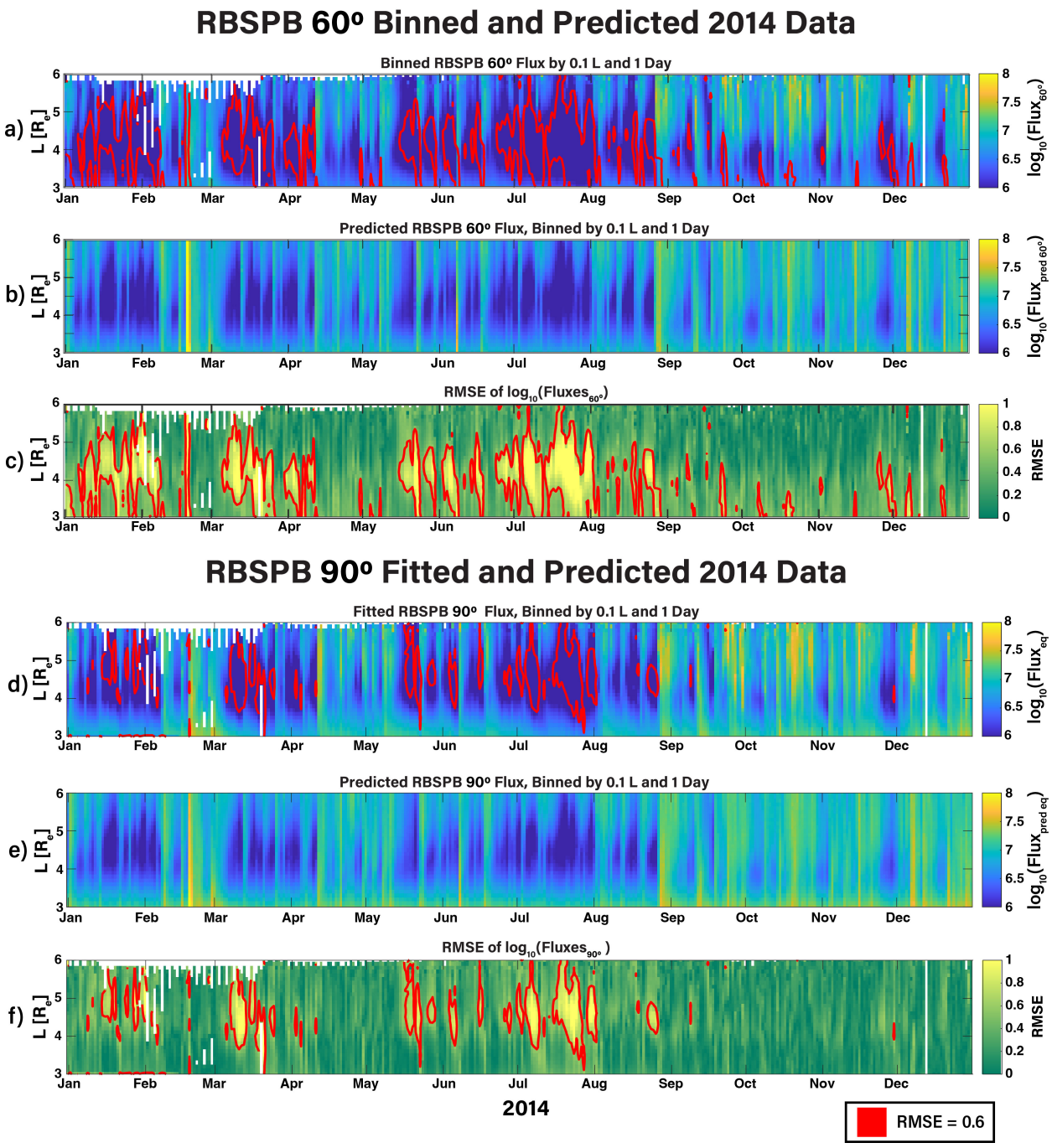

Figure 5. Equatorial Flux Results for the year 2014. The top 3 panels represent RBSPB's (a) observed 60° Flux (b) predicted 60° Flux, and (c) RMSE between (a) and (b) data. The bottom 3 panels represent RBSPB's (d) fitted 90° Flux, (e) predicted 90° Flux, and (f) RMSE between (d) and (e) data. RBSPB's observed data from 2014 is out-of-sample and fitted to a $J_D = \mathrm{C} \cdot \sin^N \alpha$ function whereas predicted data is reconstructed in a similar form from the ANN model's C and N outputs. The RBSPB fitted 90° Flux (d) are filtered by $R^2 > 0.8$. The red contours highlight RMSE = 0.6 for the 60° and 90° Flux.

357 To further assess the agreement between the observed, fitted, and predicted data, we bin
358 and average the electron flux measurements within 0.1-L and 1-day bins. We plot the coefficient
359 of determination (R^2) as a function of L-shell (Figure 6a). The model's performance peaks at R^2
360 = 0.9 for the L-shell values containing the highest outer radiation belt fluxes, $4 < L < 5.5$, for
361 both $\alpha = 60°$ and $\alpha = 90°$. We plot the mean absolute percent error (MAPE) as a function of L-
362 shell (6b) in linear space as defined in Morley et al., (2018). The MAPE for $\alpha = 60°$ is a factor of
363 ~2 higher for $3 < L < 4$ and then similar for $L > 4.5$ when compared to the MAPE for $\alpha = 90$.
364 Both profiles peak MAPE ~200 - 300% around L = 4.5, a region that the predicted flux is not as
365 low as the observed and fitted flux. With the coefficient of determination and MAPE peaking at
366 the same $L \approx 4.5$, the large, corresponding errors could be the result of differencing two small
367 flux levels that have a higher degree of uncertainty and may suggest the need more training on
368 quiet times (especially considering the solar cycle was in its declining phase for the years 2015-
369 2019). We note that there is additional source of uncertainty added from the fitting process for
370 figures 5d-f, when $\alpha = 90°$.

371 We investigate the flux measurements further by plotting the magnitude of the (6c)
372 observed 60° flux against the predicted 60° flux and the (6d) fitted 90° flux against the predicted
373 90° flux. In figure 6c, the highest L-shell values correspond to the highest magnitude of fluxes.
374 The linear relationship for figure 6c is defined as $y = 1.35x - 2.73$ with a coefficient of
375 determination of $R^2 = 0.82$. In figure 6d, the AE values positively correlate with the magnitude
376 of fluxes. The linear relationship for figure 6d is defined as $y = 1.27x - 2.14$ with a coefficient of
377 determination of $R^2 = 0.83$. Both out-of-sample comparisons (6c and 6d) indicates good
378 agreement between the model's predictions and observations.

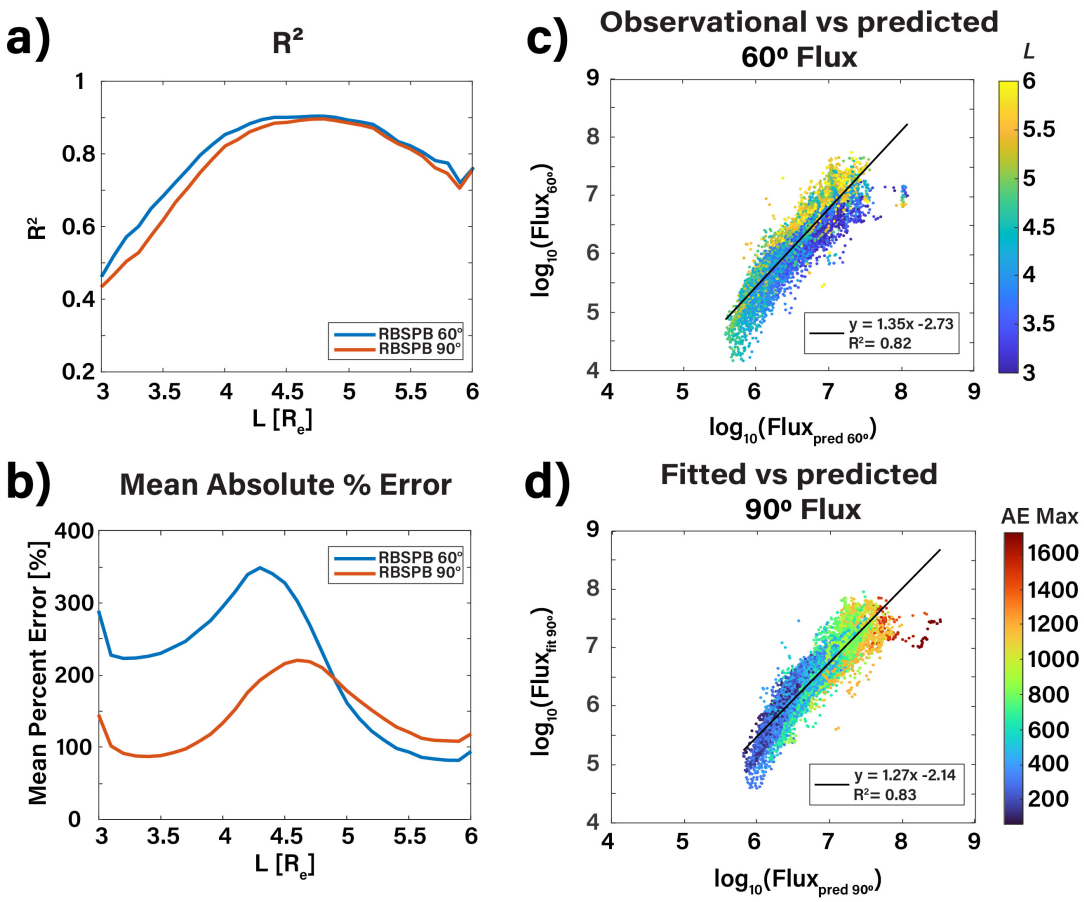

Figure 6. Error Metrics of the ANN model for the year 2014. For panels (a) and (b), RBSPB 60° Flux is represented in blue and RBSPB 90° Flux in red. (a) Coefficient of Determination as a function of L-shell. (b) Mean Absolute Percent Error (MAPE) as a function of L-shell. (c) Comparison of the observed and predicted $\log_{10}(Flux_{60°})$, flux at $\alpha = 60°$. The data is colored by L-shell. The linear relationship is defined as $y = 1.35x\text{-}2.73$ with $R^2 = 0.82$. (d) Comparison of the fitted and predicted $\log_{10}(Flux_{90°})$, flux at α_{eq}. The data is colored by AE max. The linear relationship is defined as $y = 1.27x\text{-}2.14$ with $R^2 = 0.83$.

4 Conclusions

Here we describe the development of an ANN model that is able to accurately predict in situ, equatorial fluxes and PADs based only on LEO fluxes, location of observation, and the AE geomagnetic index. We produce a conjunction dataset of 64,200 conjunctions between the equatorial, high altitude GTO RBSP satellite, and the polar LEO POES spacecraft. This conjunction dataset serves as our training set for developing an ANN model to predict RBSP PADs based only on the coincident POES fluxes (which cover only a small fraction of the PAD

near the loss-cone). We show that our ANN accurately predicts GTO electron flux measurements at 60° and 90° pitch angles, across the entire PAD, with high errors occurring only in regions with very low fluxes, which are of less importance from a space weather hazards perspective. The ANN model is able to reconstruct GTO fluxes at POES' time cadence (2 seconds) for the out-of-sample data from year 2014 which was withheld from training and represents a range of geomagnetic conditions. This ability of the ANN model indicates that the model can be used in the reconstruction of equatorial electron flux measurements for times without RBSP data (e.g., before or after RBSP's launch or time of missing or null data).

The implications arising from this work are that the type of in situ, high energy electron fluxes observed by a relatively large, expensive, and complex missions such as RBSP can be predicted with high accuracy from the relatively low-cost, simple LEO missions as demonstrated with the POES satellite. Using the remaining four POES spacecraft (e.g., Evans, 2000; Green, 2013; Green et al., 2021), it is immediately possible to create a similar model with existing data that is able to resolve MLT in several bins. This work also suggests that real-time, operational monitoring of the radiation belts with high temporal and spatial resolution could be readily achieved in the future with a constellation of low-cost CubeSats (similar to ELFIN; Angelopoulos et al., (2020)) deployed at LEO orbits, combined with the type of ML model presented in this paper to infer equatorial fluxes and PADs across a range of energies.

Acknowledgments

Processing and analysis of the MagEIS data was supported by Energetic Particle, Composition, and Thermal Plasma (RBSP-ECT) investigation funded under NASA's Prime contract no. NAS5-01072. JB and DS would like to gratefully acknowledge that this work has been supported by NSF 2025706 and NASA 80NSSC24K0240. DS would like to thank Sarah Worden, Opal Issan, and Alexander Lozinski for their assistance in evaluating this paper.

Open Research

The RBSP/MagEIS 'release 4 (rel04)' level 3 data are publicly accessible at https://rbspgway.jhuapl.edu/. The POES/MetOp data are publicly accessible at https://www.ngdc.noaa.gov/stp/satellite/poes/dataaccess.html. The OMNI data are publicly

accessible at https://cdaweb.gsfc.nasa.gov/. All files and data necessary to run the model can be accessed in the associated zenodo archive at https://doi.org/10.5281/zenodo.10627835.

References

Angelopoulos, V., Tsai, E., Bingley, L., Shaffer, C., Turner, D. L., Runov, A., et al. (2020). The ELFIN Mission. *Space Science Reviews*, *216*(5), 103. https://doi.org/10.1007/s11214-020-00721-7

Blake, J. B., Carranza, P. A., Claudepierre, S. G., Clemmons, J. H., Crain, W. R., Dotan, Y., et al. (2013). The Magnetic Electron Ion Spectrometer (MagEIS) Instruments Aboard the Radiation Belt Storm Probes (RBSP) Spacecraft. *Space Science Reviews*, *179*(1), 383–421. https://doi.org/10.1007/s11214-013-9991-8

Bortnik, J., Li, W., Thorne, R. M., & Angelopoulos, V. (2016). A unified approach to inner magnetospheric state prediction. *Journal of Geophysical Research: Space Physics*, *121*(3), 2423–2430. https://doi.org/10.1002/2015JA021733

Botek, E., Pierrard, V., & Winant, A. (2023). Prediction of Radiation Belts Electron Fluxes at a Low Earth Orbit Using Neural Networks With PROBA-V/EPT Data. *Space Weather*, *21*(7), e2023SW003466. https://doi.org/10.1029/2023SW003466

Boyd, A. J., Green, J. C., O'Brien, T. P., & Claudepierre, S. G. (2023). Specifying High Altitude Electrons Using Low-Altitude LEO Systems: Updates to the SHELLS Model. *Space Weather*, *21*(3), e2022SW003338. https://doi.org/10.1029/2022SW003338

Camporeale, E. (2019). The Challenge of Machine Learning in Space Weather: Nowcasting and Forecasting. *Space Weather*, *17*(8), 1166–1207. https://doi.org/10.1029/2018SW002061

Chen, H., Gao, X., Lu, Q., & Tsurutani, B. T. (2023). Global Distribution of Relativistic Electron Precipitation and the Dependences on Substorm Injection and Solar Wind Ram Pressure:

445 Long-Term POES Observations. *Journal of Geophysical Research: Space Physics*,
446 *128*(11), e2023JA031566. https://doi.org/10.1029/2023JA031566
447 Chen, Y., Reeves, G. D., Fu, X., & Henderson, M. (2019). PreMevE: New Predictive Model for
448 Megaelectron-Volt Electrons Inside Earth's Outer Radiation Belt. *Space Weather*, *17*(3),
449 438–454. https://doi.org/10.1029/2018SW002095
450 Chu, X., Ma, D., Bortnik, J., Tobiska, W. K., Cruz, A., Bouwer, S. D., et al. (2021). Relativistic
451 Electron Model in the Outer Radiation Belt Using a Neural Network Approach. *Space*
452 *Weather*, *19*(12), e2021SW002808. https://doi.org/10.1029/2021SW002808
453 Claudepierre, S. G., & O'Brien, T. P. (2020). Specifying High-Altitude Electrons Using Low-
454 Altitude LEO Systems: The SHELLS Model. *Space Weather*, *18*(3), e2019SW002402.
455 https://doi.org/10.1029/2019SW002402
456 Claudepierre, S. G., O'Brien, T. P., Blake, J. B., Fennell, J. F., Roeder, J. L., Clemmons, J. H., et
457 al. (2015). A background correction algorithm for Van Allen Probes MagEIS electron
458 flux measurements. *Journal of Geophysical Research: Space Physics*, *120*(7), 5703–
459 5727. https://doi.org/10.1002/2015JA021171
460 Claudepierre, S. G., Blake, J. B., Boyd, A. J., Clemmons, J. H., Fennell, J. F., Gabrielse, C., et al.
461 (2021). The Magnetic Electron Ion Spectrometer: A Review of On-Orbit Sensor
462 Performance, Data, Operations, and Science. *Space Science Reviews*, *217*(8), 80.
463 https://doi.org/10.1007/s11214-021-00855-2
464 DeForest, S. E. (1972). Spacecraft charging at synchronous orbit. *Journal of Geophysical*
465 *Research (1896-1977)*, *77*(4), 651–659. https://doi.org/10.1029/JA077i004p00651

Evans, D. S. (2000). *Polar orbiting environmental satellite space environment monitor-2 : instrument description and archive data* (No. NOAA: 19636). Retrieved from https://repository.library.noaa.gov/view/noaa/19636

Fukata, M., Taguchi, S., Okuzawa, T., & Obara, T. (2002). Neural network prediction of relativistic electrons at geosynchronous orbit during the storm recovery phase: effects of recurring substorms. *Annales Geophysicae*, *20*(7), 947–951. https://doi.org/10.5194/angeo-20-947-2002

Fung, S. F., Boscher, D. M., Bilitza, D., Tan, L. C., & Cooper, J. F. (1996). Modelling the Low-Altitude Trapped Radiation Environment, *392*, 65. Presented at the Environment Modeling for Space-Based Applications.

Greeley, A. D., Kanekal, S. G., Schiller, Q., Blum, L., Halford, A., Murphy, K., et al. (2024). Persistent Pitch Angle Anisotropies of Relativistic Electrons in the Outer Radiation Belts. *Journal of Geophysical Research: Space Physics*, *129*(1), e2023JA031549. https://doi.org/10.1029/2023JA031549

Green, J. C. (2013). *MEPED telescope data processing algorithm theoretical basis document.* National Oceanic and Atmospheric Administration. Space Environment Centre.

Green, J. C., O'Brien, T. P., Claudepierre, S. G., & Boyd, A. J. (2021). Removing Orbital Variations From Low Altitude Particle Data: Method and Application. *Space Weather*, *19*(2), e2020SW002638. https://doi.org/10.1029/2020SW002638

Gu, X., Zhao, Z., Ni, B., Shprits, Y., & Zhou, C. (2011). Statistical analysis of pitch angle distribution of radiation belt energetic electrons near the geostationary orbit: CRRES observations. *Journal of Geophysical Research: Space Physics*, *116*(A1). https://doi.org/10.1029/2010JA016052

Hornik, K., Stinchcombe, M., & White, H. (1989). Multilayer feedforward networks are universal approximators. *Neural Networks*, *2*(5), 359–366. https://doi.org/10.1016/0893-6080(89)90020-8

Jaynes, A. N., Baker, D. N., Singer, H. J., Rodriguez, J. V., Loto'aniu, T. M., Ali, A. F., et al. (2015). Source and seed populations for relativistic electrons: Their roles in radiation belt changes. *Journal of Geophysical Research: Space Physics*, *120*(9), 7240–7254. https://doi.org/10.1002/2015JA021234

Kanekal, S. G., Baker, D. N., & Blake, J. B. (2001). Multisatellite measurements of relativistic electrons: Global coherence. *Journal of Geophysical Research: Space Physics*, *106*(A12), 29721–29732. https://doi.org/10.1029/2001JA000070

Kingma, D. P., & Ba, J. (2017, January 29). Adam: A Method for Stochastic Optimization. arXiv. https://doi.org/10.48550/arXiv.1412.6980

Kitamura, K., Nakamura, Y., Tokumitsu, M., Ishida, Y., & Watari, S. (2011). Prediction of the electron flux environment in geosynchronous orbit using a neural network technique. *Artificial Life and Robotics*, *16*(3), 389–392. https://doi.org/10.1007/s10015-011-0957-1

Koons, H. C., & Gorney, D. J. (1991). A neural network model of the relativistic electron flux at geosynchronous orbit. *Journal of Geophysical Research: Space Physics*, *96*(A4), 5549–5556. https://doi.org/10.1029/90JA02380

Lanzerotti, L. J., Breglia, C., Maurer, D. W., Johnson, G. K., & Maclennan, C. G. (1998). Studies of spacecraft charging on a geosynchronous telecommunications satellite. *Advances in Space Research*, *22*(1), 79–82. https://doi.org/10.1016/S0273-1177(97)01104-6

Lazaro, D., Sicard, A., Caron, P., Falguère, D., Ecoffet, R., Standarovski, D., et al. (2022). Infer Electron Space Environment Along EOR Mission Profile From LEO Measurements: Application to EUTELSAT 7C. *IEEE Transactions on Nuclear Science*, *69*(7), 1565–1573. https://doi.org/10.1109/TNS.2022.3153081

Li, W., & Hudson, M. k. (2019). Earth's Van Allen Radiation Belts: From Discovery to the Van Allen Probes Era. *Journal of Geophysical Research: Space Physics*, *124*(11), 8319–8351. https://doi.org/10.1029/2018JA025940

Ling, A. G., Ginet, G. P., Hilmer, R. V., & Perry, K. L. (2010). A neural network–based geosynchronous relativistic electron flux forecasting model. *Space Weather*, *8*(9). https://doi.org/10.1029/2010SW000576

Lyons, L. R., Thorne, R. M., & Kennel, C. F. (1972). Pitch-angle diffusion of radiation belt electrons within the plasmasphere. *Journal of Geophysical Research (1896-1977)*, *77*(19), 3455–3474. https://doi.org/10.1029/JA077i019p03455

Ma, D., Chu, X., Bortnik, J., Claudepierre, S. G., Tobiska, W. K., Cruz, A., et al. (2022). Modeling the Dynamic Variability of Sub-Relativistic Outer Radiation Belt Electron Fluxes Using Machine Learning. *Space Weather*, *20*(8), e2022SW003079. https://doi.org/10.1029/2022SW003079

Mauk, B. H., Fox, N. J., Kanekal, S. G., Kessel, R. L., Sibeck, D. G., & Ukhorskiy, A. (2013). Science Objectives and Rationale for the Radiation Belt Storm Probes Mission. *Space Science Reviews*, *179*(1), 3–27. https://doi.org/10.1007/s11214-012-9908-y

McIlwain, C. E. (1961). Coordinates for mapping the distribution of magnetically trapped particles. *Journal of Geophysical Research (1896-1977)*, *66*(11), 3681–3691. https://doi.org/10.1029/JZ066i011p03681

534 Morley, S. K., Brito, T. V., & Welling, D. T. (2018). Measures of Model Performance Based On
535 the Log Accuracy Ratio. *Space Weather*, *16*(1), 69–88.
536 https://doi.org/10.1002/2017SW001669
537 Olson, W. P., & Pfitzer, K. A. (1977). *Magnetospheric Magnetic Field Modeling* (Tech. Rep.
538 No. Annual Report). Huntington Beach, CA: McDonnell-Douglas Astronautics Co.
539 Retrieved from https://apps.dtic.mil/sti/citations/ADA037492
540 Pedregosa, F., Varoquaux, G., Gramfort, A., Michel, V., Thirion, B., Grisel, O., et al. (2011).
541 Scikit-learn: Machine Learning in Python. *Journal of Machine Learning Research*,
542 *12*(85), 2825–2830.
543 Pires de Lima, R., Chen, Y., & Lin, Y. (2020). Forecasting Megaelectron-Volt Electrons Inside
544 Earth's Outer Radiation Belt: PreMevE 2.0 Based on Supervised Machine Learning
545 Algorithms. *Space Weather*, *18*(2), e2019SW002399.
546 https://doi.org/10.1029/2019SW002399
547 Reeves, G. D., McAdams, K. L., Friedel, R. H. W., & O'Brien, T. P. (2003). Acceleration and
548 loss of relativistic electrons during geomagnetic storms. *Geophysical Research Letters*,
549 *30*(10). https://doi.org/10.1029/2002GL016513
550 Reeves, G. D., Friedel, R. H. W., Larsen, B. A., Skoug, R. M., Funsten, H. O., Claudepierre, S.
551 G., et al. (2016). Energy-dependent dynamics of keV to MeV electrons in the inner zone,
552 outer zone, and slot regions. *Journal of Geophysical Research: Space Physics*, *121*(1),
553 397–412. https://doi.org/10.1002/2015JA021569
554 Rodger, C. J., Carson, B. R., Cummer, S. A., Gamble, R. J., Clilverd, M. A., Green, J. C., et al.
555 (2010b). Contrasting the efficiency of radiation belt losses caused by ducted and

nonducted whistler-mode waves from ground-based transmitters. *Journal of Geophysical Research: Space Physics*, *115*(A12). https://doi.org/10.1029/2010JA015880

Rodger, C. J., Clilverd, M. A., Green, J. C., & Lam, M. M. (2010a). Use of POES SEM-2 observations to examine radiation belt dynamics and energetic electron precipitation into the atmosphere. *Journal of Geophysical Research: Space Physics*, *115*(A4). https://doi.org/10.1029/2008JA014023

Schulz, M., & Lanzerotti, L. J. (1974). *Particle Diffusion in the Radiation Belts* (Vol. 7). Springer.

Sinha, S., Chen, Y., Lin, Y., & Pires de Lima, R. (2021). PreMevE Update: Forecasting Ultra-Relativistic Electrons Inside Earth's Outer Radiation Belt. *Space Weather*, *19*(9), e2021SW002773. https://doi.org/10.1029/2021SW002773

Spence, H. E., Reeves, G. D., Baker, D. N., Blake, J. B., Bolton, M., Bourdarie, S., et al. (2013). Science Goals and Overview of the Radiation Belt Storm Probes (RBSP) Energetic Particle, Composition, and Thermal Plasma (ECT) Suite on NASA's Van Allen Probes Mission. *Space Science Reviews*, *179*(1), 311–336. https://doi.org/10.1007/s11214-013-0007-5

Thorne, R. M., Li, W., Ni, B., Ma, Q., Bortnik, J., Chen, L., et al. (2013). Rapid local acceleration of relativistic radiation-belt electrons by magnetospheric chorus. *Nature*, *504*(7480), 411–414. https://doi.org/10.1038/nature12889

Tsyganenko, N. A. (1989). A magnetospheric magnetic field model with a warped tail current sheet. *Planetary and Space Science*, *37*, 5–20. https://doi.org/10.1016/0032-0633(89)90066-4

578 Vampola, A. L. (1997). Outer zone energetic electron environment update. In *Conference on the*
579 *High Energy Radiation Background in Space. Workshop Record* (pp. 128–136).
580 https://doi.org/10.1109/CHERBS.1997.660263
581 Van Allen, J. A., Ludwig, G. H., Ray, E. C., & McIlwain, C. E. (1958). Observation of High
582 Intensity Radiation by Satellites 1958 Alpha and Gamma. *Journal of Jet Propulsion*,
583 *28*(9), 588–592. https://doi.org/10.2514/8.7396
584 Yang, X., & Wang, L. (2021). A Study of the Performances of Widely Used External Magnetic
585 Field Models in the Outer Zone of the Earth's Radiation Belts by Comparing the Field
586 Observations From Van Allen Probe-A and the Model Estimations. *Space Weather*,
587 *19*(12), e2021SW002722. https://doi.org/10.1029/2021SW002722
588 Zhelavskaya, I. S., Aseev, N. A., & Shprits, Y. Y. (2021). A Combined Neural Network- and
589 Physics-Based Approach for Modeling Plasmasphere Dynamics. *Journal of Geophysical*
590 *Research: Space Physics*, *126*(3), e2020JA028077.
591 https://doi.org/10.1029/2020JA028077
592